The polarization of microglia and infiltrated macrophages in the injured mice spinal cords: A dynamic analysis

Jing-Lu Li [Equal first author, 1, 2], **Gui-Qiang Fu** [Equal first author, 1, 2], **Yang-Yang Wang** [1, 2], **Ming-Ming Bian** [1, 2], **Yao-Mei Xu** [1, 2], **Lin Zhang** [1, 2], **Yu-Qing Chen** [1, 2], **Nan Zhang** [1, 2], **Shu-Qin Ding** [1, 2], **Rui Wang** [2], **Rui Fang** [3], **Jie Tang** [2], **Jian-Guo Hu** [Corresp., 1, 2], **He-Zuo Lü** [Corresp. 1, 2]

[1] Clinical Laboratory, the First Affiliated Hospital of Bengbu Medical College, Bengbu, China

[2] Anhui Key Laboratory of Tissue Transplantation, the First Affiliated Hospital of Bengbu Medical College, Bengbu, China

[3] Department of Clinical Medical, Bengbu Medical College, Bengbu, China

Corresponding Authors: Jian-Guo Hu, He-Zuo Lü
Email address: jghu9200@163.com, lhz233003@163.com

Background. Following spinal cord injury (SCI), a large number of peripheral monocytes infiltrate into the lesion area and differentiate into macrophages (Mø). These monocyte-derived Mø are very difficult to distinguish from the local activated microglia (MG). Therefore, the term Mø/MG are often used to define the infiltrated Mø and/or activated MG. It has been recognized that pro-inflammatory M1-type Mø/MG play "bad " roles in the SCI pathology. Our recent research showed that local M1 cells are mainly $CD45^{-/low}CD68^{+}CD11b^{+}$ in the subacute stage of SCI. Thus, we speculated that the M1 cells in injured spinal cords mainly derived from MG rather than infiltrating Mø. So far, their dynamics following SCI are not yet entirely clear. **Methods.** The female C57BL/6 mice were used to establish SCI model, using an Infinite Horizon impactor with a 1.3 mm diameter rod and a 50 Kdynes force. Sham-operated (sham) mice only underwent laminectomy without contusion. Flow cytometry and immunohistofluorescence were combined to analyze the dynamic changes of polarized Mø and MG in the acute (1 day), subacute (3, 7 and 14 days) and chronic (21 and 28 days) phases of SCI. **Results.** The total Mø/MG gradually increased and peaked at 7 days post-injury (dpi), and maintained at high levels 14, 21 and 28 dpi. Most of the Mø/MG were activated, and the Mø increased significantly at 1 and 3 dpi. However, with the pathological process, activated MG increased nearly to 90% at 7, 14, 21 and 28 dpi. Both M1 and M2 Mø were increased significantly at 1 and 3 dpi. However, they decreased to very low levels from 7 to 28 dpi. On the contrary, the M2-type MG decreased significantly following SCI and maintained at a low level during the pathological process.

The polarization of microglia and infiltrated macrophages in the injured mice spinal cords: A dynamic analysis

Jing-Lu Li[1, 2&], Gui-Qiang Fu[1, 2&], Yang-Yang Wang[1, 2], Ming-Ming Bian[1, 2], Yao-Mei Xu[1, 2], Lin Zhang[1, 2], Yu-Qing Chen[1, 2], Nan Zhang[1, 2], Shu-Qin Ding[1, 2], Rui Wang[2], Rui Fang[3], Jie Tang[2], Jian-Guo Hu[1, 2*], He-Zuo Lü[1, 2*]

[1] Clinical Laboratory, the First Affiliated Hospital of Bengbu Medical College, Bengbu, Anhui 233004, P.R. China

[2] Anhui Key Laboratory of Tissue Transplantation, the First Affiliated Hospital of Bengbu Medical College, Bengbu, Anhui 233004, P.R. China

[3] Department of Clinical Medical, Bengbu Medical College, Bengbu, Anhui 233030, P.R. China

[&] These authors contributed equally to this work

*Co-corresponding authors:

Jian-Guo Hu

Email address: jghu9200@163.com

He-Zuo Lü

Email address: lhz233003@163.com

Please address correspondence to:

He-Zuo Lü, M.D. Ph.D., Professor

Anhui Key Laboratory of Tissue Transplantation

the First Affiliated Hospital of Bengbu Medical College

287 Chang Huai Road

Bengbu 233004, P.R. China

Tel: +86-552-3170692

E-mail: lhz233003@163.com

Abstract

Background. Following spinal cord injury (SCI), a large number of peripheral monocytes infiltrate into the lesion area and differentiate into macrophages (Mø). These monocyte-derived Mø are very difficult to distinguish from the local activated microglia (MG). Therefore, the term Mø/MG are often used to define the infiltrated Mø and/or activated MG. It has been recognized that pro-inflammatory M1-type Mø/MG play "bad " roles in the SCI pathology. Our recent research showed that local M1 cells are mainly $CD45^{-/low}CD68^{+}CD11b^{+}$ in the subacute stage of SCI. Thus, we speculated that the M1 cells in injured spinal cords mainly derived from MG rather than infiltrating Mø. So far, their dynamics following SCI are not yet entirely clear.
Methods. The female C57BL/6 mice were used to establish SCI model, using an Infinite Horizon impactor with a 1.3 mm diameter rod and a 50 Kdynes force. Sham-operated (sham) mice only underwent laminectomy without contusion. Flow cytometry and immunohistofluorescence were combined to analyze the dynamic changes of polarized Mø and MG in the acute (1 day), subacute (3, 7 and 14 days) and chronic (21 and 28 days) phases of SCI.
Results. The total Mø/MG gradually increased and peaked at 7 days post-injury (dpi), and maintained at high levels 14, 21 and 28 dpi. Most of the Mø/MG were activated, and the Mø increased significantly at 1 and 3 dpi. However, with the pathological process, activated MG increased nearly to 90% at 7, 14, 21 and 28 dpi. Both M1 and M2 Mø were increased significantly at 1 and 3 dpi. However, they decreased to very low levels from 7 to 28 dpi. On the contrary, the M2-type MG decreased significantly following SCI and maintained at a low level during the pathological process.

Introduction

Spinal cord injury (SCI) is a serious neurological disorder, which caused by traffic accidents, trauma and other reasons (Attal 2021; Perrouin-Verbe et al. 2021; Quadri et al. 2020). As the bridge of brain and peripheral nerves, the nerve fibers of spinal cord are distributed to the skin, muscles and various internal organs. 0nce damaged, it will cause serious pathophysiological dysfunctions. For patients, SCI will cause serious physical and mental suffering. The disease also causes serious economic and social burdens. (Chay & Kirshblum 2020). Therefore, to find effective treatment strategies, its pathological mechanism should be deeply explored.

The pathological process of SCI includes primary injury and secondary injury. Primary injury refers to the direct injury of mechanical force to spinal cord. Secondary injury is triggered by primary injury, which includes local vascular disorder, edema, ischemia, free radical reaction, electrolyte change, inflammation, axon necrosis and demyelination, fibroglial scar and cyst formation (Anjum et al. 2020; Zhang et al. 2021).

Inflammation is one of the important mechanisms of secondary pathological damage of SCI (Mallon et al. 2021). After SCI, with the destruction of blood spinal cord barrier, MG are activated, the inflammatory factors and chemokines are increased, and the peripheral immune cells infiltrate into the injured spinal cord to form an immune microenvironment, resulting in neuronal death and demyelination (Brockie et al. 2021; Rezvan et al. 2020; Shields et al. 2020). Following SCI, the different immune cell subsets with different functions affect the local immune microenvironment by producing different cytokines (Mishra et al. 2021). Previous studies have reported that in the injured spinal cord, the cellular components include locally activated MG, infiltrated Mø, lymphocytes, neutrophils, dendritic cells, etc., and these cells are divided into different subsets, some are neuroprotective, while others have neurodamaging

effects (Hu et al. 2016; Ma et al. 2015; Milich et al. 2021). Moreover, neurodamaging subsets (e.g., M1, Th1, Th17, etc.) are dominant, which is an important pathological mechanism of SCI (Chen et al. 2021; Chen et al. 2020). However, which of these complex immune cell populations plays a key role? So far, there is still no final conclusion.

Following SCI, a large number of peripheral blood-derived monocytes infiltrate into the injured spinal cord and differentiate into Mø, which are indistinguishable from the local MG, therefore the term Mø/MG was often used to define the infiltrated Mø and/or activated MG in the literatures (Fan et al. 2020; Gao et al. 2021; Rismanbaf et al. 2021). However, as research technology advances by leaps and bounds, the peripheral infiltrated Mø and locally activated MG can be identified (Chen et al. 2021; Chen et al. 2020; Milich et al. 2021). Our recent studies have found that proinflammatory M1 cells are absolutely dominant at 7 dpi following SCI, and these cells mainly from MG rather than peripheral infiltrated Mø (Chen et al. 2021; Chen et al. 2020). This suggests that M1 cells derived from MG might be the key inflammatory cells in the immune microenvironment of injured spinal cords. However, the dynamic patterns of MG, infiltrated Mø and their subsets during the whole pathological process of SCI are still unclear. Therefore, the purpose of this study was to explore the dynamic patterns of these cells following SCI using the strategy of combining flow cytometry (FCM) and immunohistofluorescence (IHF).

Materials & Methods

Animals

A total of 150 specific-pathogen free adult female C57BL/6 mice (18–20 g) were obtained from Chang Zhou Cavens Laboratory Animal Ltd. (Chang Zhou, China; license No. SCXK (Su) 2016-0010). Animal were housed as previously described (Chen et al. 2021; Chen et al. 2020). All experimental designs and reports were referred to previous to the previous guidelines (Kilkenny et al. 2011). The surgery protocol was approved by the Animal Care Ethics Committee of Bengbu Medical College. The number of Animal Ethical Approval was 2017-037. The mice were randomly divided into sham-operated (sham), 1-, 3-, 7-, 14-, 21- and 28-days post-injury (dpi) groups, using a computer based random order generator (Zhao et al. 2018). The comprehensive description of the total number of mice used is shown in Figure 1.

Contusive SCI

The mice contusive SCI model was established as described previously(Chen et al. 2021; Chen et al. 2020). Specifically, the Infinite Horizon impactor was made by Precision Systems & Instrumentation (Lexington, KY, USA). Anesthetics (80 mg/kg ketamine and 10 mg/kg xylazine) for intraperitoneal injection were obtained from Sigma-Aldrich (St. Louis, MO, USA). The T9 spinal cord was impacted with 50Kdynes force, and the diameter of the impact rod was 1.3 mm. After impact, the spinal cord was filled with blood and edema. Sham-operated mice only underwent laminectomy without contusion. After operation, the animal care and welfare were performed as previously described (Chen et al. 2021; Chen et al. 2020), which included bladder emptying three times per day, relieving pain with meloxicam (5mg/kg, CSN pharm, IL, USA), and preventing infection with chloramphenicol (50mg/kg, Sangon Biotech, Shanghai, China) for 7 days after surgery. Inclusion criteria: the animals were undergoing successful contusive SCI, defined by the T9 site was filled with blood and edema, and the spinal cord was intact and not ruptured. Exclusion criteria: the degree of injury is not up to the standard, postoperative infection or sacrifice.

Flow cytometry

At the indicated time points post-injury, the samples were collected and single-cell suspensions were obtained using Percoll gradient centrifugation as previously described (Chen et al. 2021; Chen et al. 2020). Briefly, the chest cavity was opened with surgical scissors to expose the heart. The ventricle was clamped with a vascular clamp to fix the heart. The No.7 needle was inserted into the left ventricle. At the same time, a small opening was cut on the right atrium so that the blood and lavage solution can be drained. Then, 10ml of 0.01M phosphate-buffered saline (PBS) buffer solution (pH = 7.4) was slowly injected at 250 ml/h with a microinjection pump. After perfusion, the 5 mm spinal cord segments which contained the injury center were taken, and the corresponding spinal cord segments were also obtained from sham group. The spinal cords were put into the 45-μm nylon mesh and fully ground with the syringe plunger to obtain single cell suspensions. To obtain enough cells for analysis, 3 spinal cord segments were mixed for one test. The Percoll gradient centrifugation (Amersham Pharmacia Biotech, Piscataway, NJ, USA) was used to separate the single cells. Table 1 showed the fluorescent labeled antibodies used in this study to identify different immune cell subtypes. To eliminate the background staining caused by the non-specific binding of the antibody, the immunoglobulin with the same species, subtype, dose and fluorescein as the primary antibody was used as the isotype control. The cells were collected using a BD Accuri flow cytometer (Becton Dickinson, San Diego, CA, USA), and the data were analyzed using FlowJo7.6.1 software (FlowJo, LLC, Ashland, OR, USA).

Immunofluorescence double-staining

At the indicated time points post-injury, mice were euthanized perfused with PBS as described in "Flow cytometry". Then, the mice were perfused with 10 mL of 4% paraformaldehyde (PFA) at a rate of 180 mL/h. After perfusion, the 5 mm spinal cord segments which contained the injury center were collected and fixed in 10 mL of 4% PFA solution at 4°C overnight. The next day, the spinal cords were removed from 4% PFA solution and placed in 20% sucrose solution (prepared in PBS) at 4°C overnight. The third day, the spinal cords were transferred to 30% sucrose at 4°C, until the samples sinking to the bottom. This process usually needs one day. Next, the embedding agent (Tissue-Tek, Sakura Finetek USA Inc., Torrance, CA, USA) was used to embed the spinal cord segments at -20°C. The 6 μm thick transverse sections were cut using a Leica CM1900 cryostat (Leica Microsystems, Bannockburn, IL, USA). The IHF assay was performed as previously described (Chen et al. 2021; Chen et al. 2020). Briefly, the slides were washed three times with 0.01 M PBS to completely clear the embedding agent. When the slides were left to dry, the blocking solution (0.01 M PBS containing 10% normal goat serum) were used for 2 hours at room temperature to eliminate the background staining caused by the non-specific binding of antibodies. After cleaning the blocking solution, the primary antibodies with appropriate concentration were incubated overnight at 4°C. The next day, the slides were washed three times with 0.01 M PBS to completely remove the unbound antibodies. Then, the secondary antibodies with appropriate concentration were incubated at 37°C for 1 hour. The primary and FITC and RHO-conjugated secondary antibodies were shown in Table 1. After the second antibody incubation, the 0.01 M PBS was used to wash the slides for three times, and the 1 μg/ml Hoechst 33342 (Sigma-Aldrich; Cat# B2261) containing medium was used to coverslip the slides. Finally, the slides were examined using a ZWISS Axio observation microscope (Carl Zeiss, Oberkochen, Germany). The cell quantification was performed as previously described (Chen et al. 2021; Chen et al. 2020). Specifically, for each spinal cord, the cells of 5 complete cross-sections containing the injury epicenter (0 mm), rostral (1 mm and 0.5 mm) and caudal (-1 mm and -0.5 mm) were counted.

Statistical analyses

The SPSS software v.14.0 (SPSS Inc., Chicago, IL, USA) was used to statistical analysis. The non-parametric Kruskal Wallis analysis of variance (ANOVA) following by the individual Mann-Whitney U test was used. The $P < 0.05$ was considered to be statistically significant.

Results

Temporal pattern of MG and infiltrated Mø following SCI: the flow cytometry (FCM) analysis

To determine the temporal pattern of MG and infiltrated Mø, a panel of cell markers (CD11b, CD45 and CD68) was examined by FCM. Here, $CD45^{high}$ population was peripheral infiltrated leukocytes, $CD68^{+}CD11b^{+}$ population was activated Mø and MG, $CD45^{high}CD11b^{+}$ population was peripheral infiltrated Mø, $CD45^{-/low}CD11b^{+}$ population was MG, $CD45^{high}CD68^{+}CD11b^{+}$ population was activated peripheral infiltrated Mø, $CD45^{-/low}CD68^{+}CD11b^{+}$ population was activated MG, and $CD45^{high}CD68^{-}CD11b^{-}$ population was peripheral infiltrated leukocytes excluding Mø (Figure 2A).

Figure 2B showed that $CD11b^{+}$ cells had no significant difference among sham, 1 and 3 dpi groups ($P > 0.05$, $n = 6$). However, at 7 dpi, the proportion increased significantly and reached to peak, although decreasing at the later time points (14, 21 and 28 dpi), they remained at high levels comparing with sham,1 and 3 dpi groups ($P < 0.01$, $n = 6$).

Figure 2C showed that $CD68^{+}$ cells were the lowest in the sham group comparing with the injured groups ($P < 0.01$, $n = 6$). The proportions increased significantly after injury, reached to peak at 7 dpi, and maintained at high levels at 14, 21 and 28 dpi. There were no significant differences among 7, 14, 21 and 28 dpi ($P > 0.05$, $n = 6$). However, $CD68^{+}$ cells in these four groups were significant more comparing with sham, 1 and 3 dpi ($P < 0.05$ or 0.01, $n = 6$).

Figure 2D showed that $CD11b^{+}CD68^{+}$ cells were extremely rare in sham group, however, they increased significantly in the injured groups ($P < 0.01$, $n = 6$). The proportions had no significant differences between 1 and 3 dpi ($P > 0.05$, $n = 6$). However, it reached to peak at 7 dpi, and then decreased, but remained at high levels at 14, 21 and 28 dpi.

Figure 2E showed that $CD45^{high}$ cells were extremely rare in sham group, and they gradually increased after injury, peaked at 7 and 14 dpi, and then decreased, but still maintained at high levels at 21 and 28 dpi.

Figure 2F showed that $CD11b^{+}CD45^{high}$ cells were also extremely rare in sham group, and they significantly increased after injury, peaked at 7 dpi, and then decreased, but still maintained at high levels at 14, 21 and 28 dpi. The proportion of $CD11b^{+}CD45^{high}$ cells in each group is significantly lower than that of their corresponding $CD11b^{+}$ cells (Figure 2B).

Figure 2G showed that $CD11b^{+}CD45^{-/low}$ cells had no significant difference among sham, 1 and 3 dpi groups ($P > 0.05$, $n = 6$). However, at 7 dpi, the proportion increased significantly and reached a peak, although decreased at the later time points (14, 21 and 28 dpi), they still maintained at high levels comparing with sham,1 and 3 dpi groups ($P < 0.01$, $n = 6$). Except for the 1 and 3 dpi groups, $CD11b^{+}CD45^{-/low}$ cells constitute the majority of $CD11b^{+}$ cells (Figure 2B).

Figure 2H showed that $CD68^{+}CD45^{high}$ cells were also extremely rare in sham group, and they rapidly increased after injury. Up to 28 dpi, they still maintained at high levels. The proportion of $CD68^{+}CD45^{high}$ cells in each SCI group is significantly lower than that of their corresponding $CD68^{+}$ cells (Figure 2C).

Figure 2I showed that the percentages of$CD68^{+}CD45^{-/low}$ cells in sham group was the lowest comparing with the injured groups ($P < 0.05$ or 0.01, $n = 6$). The proportions had no significant

differences at 1 and 3 dpi ($P > 0.05$, $n = 6$). However, they reached to peak at 7 and 14 dpi, and remained at high levels at 21 and 28 dpi. The proportion of $CD68^+CD45^{-/low}$ cells in each SCI group is significantly lower than that of their corresponding $CD68^+$ cells (Figure 2C).

Figure 2K showed that $CD68^+CD11b^+CD45^{high}$ cells were extremely rare in sham group, and they rapidly increased after injury, peaked at 1, 3 and 7 dpi. Comparing with sham group, these cells in the 1, 3 and 7 dpi groups were significantly more ($P < 0.01$, $n = 6$). Although, comparing with 1, 3 and 7 dpi groups, the proportions decreased to the lower levels at the later time points (14, 21 and 28 dpi) ($P < 0.05$, $n = 6$), they still maintained at higher levels comparing to the sham group ($P < 0.05$, $n = 6$). Comparing with Figure 2H, the proportion of cells in Figure 2K is lower. This indicated that the activated peripheral infiltrated Mø in the injured spinal cord are significantly inferior to activated MG.

Figure 2L showed that $CD68^+CD11b^+CD^{45-/low}$ cells were also extremely rare in sham group, and they gradually increased after injury, peaked at 7 dpi, and then decreased, but still maintained at high levels at 14, 21 and 28 dpi. Comparing to sham group, the percentages of $CD68^+CD11b^+CD^{45-/low}$ cells in all SCI groups had significant differences ($P < 0.01$, $n = 6$).

Temporal pattern of MG and infiltrated Mø following SCI: the immunohistofluorescence (IHF) analysis

To verify the temporal pattern of MG and infiltrated Mø detected by FCM, the spinal cords from several representative time points after SCI (sham, 1, 7 and 28 dpi) were selected for IHF analysis. CD11b, CD68 and TMEM119 antibodies were used for immunofluorescence labeling (Figure 3). Here, $TMEM119^+CD11b^+$ cells are total MG, $TMEM119^-CD11b^+$ cells are monocyte-derived Mø, $TMEM119^+CD68^+$ cells are activated MG, $TMEM119^-CD68^+$ cells are activated monocyte-derived Mø, respectively (Figure 3A-H).

The representative images showed that $TMEM119^+CD11b^+$ cells could be detected in all groups (Figure 3A-D). The statistical results (Figure 3E) showed that the number (cells/mm^2) of $TMEM119^+CD11b^+$ cells had no significant difference between sham (117.50 ± 19.30) and 1 dpi (200.33 ± 16.59) groups ($P > 0.05$, $n = 6$). Comparing with the other three groups, there were most $TMEM119^+CD11b^+$ cells in 7 dpi (537.33 ± 99.80) ($P < 0.01$, $n = 6$). Although, the cells were decreased at 28 dpi (308.33 ± 50.27), the number still significantly more comparing with sham and 1 dpi groups ($P < 0.01$, $n = 6$). In sham group, $TMEM119^-CD11b^+$ cells were extremely rare (Figure 3A), and they significantly increased in the three SCI groups (Figure 3B-D). The statistical results (Figure 3F) showed that the numbers of $TMEM119^-CD11b^+$ cells in all three SCI groups were significant more than that of sham (70.17 ± 7.65) group ($P < 0.01$, $n = 6$). Comparing with the other three groups, there were also most $TMEM119^-CD11b^+$ cells in 7 dpi (201.80 ± 42.53) group ($P < 0.05$, $n = 6$).

In Figure 4A, both $TMEM119^+CD68^+$ and $TMEM119^-CD68^+$ cells were extremely rare in sham group. However, both of them could be detected in all SCI groups (Figure 4B-D). The statistical results (Figure 4E and F) showed that the numbers of these two types of cells had significant differences among sham and SCI groups ($P < 0.01$, $n = 6$). Comparing with the three other groups, there were most $TMEM119^+CD68^+$ cells in 7 dpi (473.50 ± 64.48) group ($P < 0.01$, $n = 6$). Although, the number of these cells decreased at 28 dpi (269.67 ± 42.49), it still significantly more comparing with sham (6.67 ± 6.31) and 1 dpi (156 ± 43.75) groups ($P < 0.01$, $n = 6$). Comparing with the other two groups, $TMEM119^-CD68^+$ cells were most in 1 (155.00 ± 18.51) and 7 dpi (124.75 ± 34.88) groups ($P < 0.01$, $n = 6$).

Temporal pattern of SCI-induced M1 and M2 differentiation of Mø and MG: the FCM analysis

To further explore the temporal pattern of SCI-induced M1 and M2 differentiation of Mø and MG, FCM was used by combining CD68, CD45, CD11b and CCR7 antibodies.

As shown in Figure 5A, the same size "region" of total $CD11b^+$ cells (R1) were set for each sample in the pseudocolor plots of CD45/CD11b, and then the percentage of each cell population was analyzed in the pseudocolor plots of CD68/CCR7 by setting the boundary between negative and positive with isotype-matched antibodies. The statistical results (Figure 5B) showed that the percentage of $CD11b^+CD68^+CCR7^+$ M1 cells in the sham group was the lowest. The proportions significantly increased after injury, reached to peak from 7 dpi, and maintained at high levels at 14, 21 and 28 dpi. There were no significant differences among 7, 14, 21 and 28 dpi ($P > 0.05$, $n = 6$). However, the percentages in these four groups were significant higher comparing with sham and 1 dpi groups ($P < 0.01$, $n = 6$).

Figure 5C showed that $CD11b^+CD68^+CCR7^-$ M2 cells had no significant differences among all groups ($P > 0.05$, $n = 6$). However, when converted to ratio (Figure 5D), the total M1/M2 ratios in all SCI groups were significant increased comparing with the sham group ($P < 0.01$, $n = 6$).

As shown in Figure 5E, in the pseudocolor plots of CD11b/CD45, the same size "region" of $CD11b^+CD45^{-/low}$ cells (R2) were set for each sample, and then the percentages of cell populations were analyzed same as Figure 5A. The statistical results (Figure 5F) showed that the percentage of $CD11b^+CD45^{-/low}CD68^+CCR7^+$ MG-derived M1 cells in sham group was the lowest comparing with the injured groups, and the differences were statistically significant ($P < 0.01$, $n = 6$). The proportions significantly increased after injury, and reached to peak at 14 and 21 dpi, and continued at high level at 28 dpi. The percentages in the groups of 3, 7, 14, 21 and 28 dpi were significantly higher than that of 1 dpi ($P < 0.05$ or 0.01, $n = 6$).

Figure 5G showed that $CD11b^+CD45^{-/low}CD68^+CCR7^-$ MG-derived M2 cells had no significant differences among all groups ($P > 0.05$, $n = 6$). However, when converted to ratio (Figure 5H), the M1/M2 ratio of MG was very low in sham group, and they increased after SCI, peaked at 7 dpi, and then decreased at 21 and 28 dpi. In the group of 7 dpi, the ratio was significantly higher than those of the other groups ($P < 0.05$, $n = 6$).

In Figure 5I, in the pseudocolor plots of CD11b/CD45, the same size "region" of $CD45^{high}CD11b^+$ cells (R3) were set for each sample, and then the percentages of cell populations were analyzed same as Figure 5A. Figure 5J showed that the percentages of $CD11b^+CD45^{high}CD68^+CCR7^+$ peripheral infiltrated M1 cells showed an increasing trend after SCI, and reached the highest levels at 28 dpi. The 7, 14, 21 and 28 dpi groups had statistically significant comparing with sham and 1dpi ($P < 0.05$ or 0.01, $n = 6$). Figure 5K showed that the percentages of $CD11b^+CD45^{high}CD68^+CCR7^-$ peripheral infiltrated M2 cells were highest at 3 and 7 dpi, which were statistically significant comparing with the other groups ($P < 0.01$, $n = 6$). When converted to ratio (Figure 5l), the infiltrated M1/M2 ratio was very low in sham group, and there was a transient rise at 1 dpi. Then, the ratios decreased to sham level at 3 and 7 dpi, and then showed an increasing trend from 14 to 28 dpi, it reached the highest levels at 28 dpi. Among sham, 3 and 7 dpi groups, the ratios had no significant differences ($P > 0.05$, $n = 6$). However, comparing with the other groups, the ratios were significant lower ($P < 0.05$ or 0.01, $n = 6$).

Temporal pattern of SCI-induced M1 and M2 differentiation of Mø and MG: the IHF analysis

In IHF analysis, $CD68^+CCR7^+$ and $CD68^+Arg1^+$ were used to label total M1 and M2 cells, respectively (Figure 6); $TMEM119^+$ $CCR7^+$ and $TMEM119^+Arg1^+$ cells were M1 and M2 MG, respectively (Figure 7A-J). Therefore, ($CD68^+CCR7^+$ minus $TMEM119^+CCR7^+$) and

(CD68$^+$Arg1$^+$ minus TMEM119$^+$Arg1$^+$) were M1 and M2 monocyte-derived Mø, respectively (Figure 7K and L).

The representative images showed that CD68$^+$CCR7$^+$, CD68$^+$Arg1$^+$, TMEM119$^+$CCR7$^+$ and TMEM119$^+$Arg1$^+$ cells were both extremely rare in sham-operated spinal cords (Figures 6A and E, 7A and E). However, these cells could be detected in all SCI groups (Figure 6B-D, F-H, and 7B-D, F-H).

The statistical results (Figure 6I) showed that in the groups of sham, 1, 7 and 28 dpi, the numbers of CD68$^+$CCR7$^+$ cells were 2.67 ± 2.50, 235.33 ± 5.13, 577.17 ± 40.18 and 543.17 ± 31.35, respectively. All SCI groups were significant more than that of sham ($P < 0.01$, $n = 6$). Up to 7 dpi, the cell number reached to peak, and continued at high levels at 28 dpi.

In Figure 6J, the numbers of CD68$^+$Arg1$^+$ cells in the groups of sham, 1, 7 and 28 dpi were 3.83 ± 3.43, 105.33 ± 9.56, 72.83 ± 10.55 and 150.17 ± 22.21, respectively. Although, CD68$^+$Arg1$^+$ cells in all SCI groups were significant more than that of sham group ($P < 0.01$, $n = 6$), the 7 dpi had the least number of cells among the three SCI groups, and there were most cells in 28 dpi group.

In Figure 7I, TMEM119$^+$CCR7$^+$ cells in the groups of sham, 1, 7 and 28 dpi were 3.17 ± 1.83, 205.17 ± 9.97, 412.33 ± 18.04 and 410.17 ± 50.92, respectively. The overall change trend was similar to that of CD68$^+$CCR7$^+$ cells. Figure 7J showed that TMEM119$^+$Arg1$^+$ cells in the groups of sham, 1, 7 and 28 dpi were 4.33 ± 2.42, 85.83 ± 10.68, 50.00 ± 4.29 and 125.00 ± 13.33, respectively. The overall trend was also similar to that of CD68$^+$Arg1$^+$ cells.

In Figure 7K, the infiltrated CD68$^+$CCR7$^+$ cells in the groups of sham, 1, 7 and 28 dpi were 0.00 ± 0.00, 30.17 ± 11.72, 164.83 ± 45.64 and 133.00 ± 56.67, respectively. All SCI groups were significant more than that of sham group ($P < 0.01$, $n = 6$). Up to 7 dpi, the cell number reached to peak. Although the number of cells had a decreasing trend, it remained at a higher level at 28 dpi. Figure 7L showed that although the infiltrated CD68$^+$Arg1$^+$ cells could be detected in SCI groups, they were very rare. The numbers in the groups of sham, 1, 7 and 28 dpi were 0.00 ± 0.00, 19.50 ± 12.65, 22.83 ± 12.04 and 25.17 ± 15.74, respectively. All three SCI groups were significant more than that of sham group ($P < 0.01$, $n = 6$).

Summary of dynamic changes of MG, infiltrated Mø and their subsets

As shown in the first row of Figure 8, the proportions of total Mø/MG in the groups of SCI were gradually increased and peaked at 7 dpi. Although, decreasing at 14, 21 and 28 dpi, they were still maintained at high levels compared with sham, 1 and 3 dpi groups.

The second row of Figure 8 showed that most of the Mø/MG were activated following SCI.

The third row of Figure 8 showed that MG were absolutely dominant and Mø were few in the sham-operated spinal cords. In the acute phase of SCI (1 and 3 dpi), the proportions of activated Mø increased significantly. However, with the progression of the SCI, the proportions of activated MG increased nearly to 90% in subacute phase (7 and 14 dpi) and chronic phase (21 and 28 dpi).

Finally, we further analyzed the proportion of M1 and M2 subsets in the activated MG and infiltrated Mø. The fourth row 4 of Figure 8 showed that in sham, 1, 3, 7, 14, 21 and 28 dpi groups, the proportions of M1 Mø were 7%, 43%, 51%, 7%, 9%, 17% and 12%, respectively, while M2 Mø were 6%, 6%, 23%, 3%, 1%, 1% and 0%, respectively. The proportions of M1 MG were 31%, 43%, 20%, 69%, 79%, 66% and 68%, respectively, and M2 MG were 56%, 8%, 6%, 21%, 11%, 16% and 20%, respectively. These results showed that there are very few peripheral Mø in the sham-operated spinal cords, while the proportion of MG is absolutely dominant, and the MG are mainly M2 subtype. In the acute phase of SCI, the proportion of

peripheral infiltrated Mø increased transiently, and M1 Mø are absolutely dominant, but in the subacute phase, M1 MG were absolutely dominant and continued to the chronic phase (28 dpi, the longest time point observed in this study).

Discussion

Following SCI, the local microenvironment of spinal cord is destroyed (Anjum et al. 2020; Fan et al. 2022; Fan et al. 2018). SCI not only leads to neuronal and oligodendrocyte necrosis and astrocyte activation, it also triggers the immune response, which includes the local MG activation and the peripheral immune cell infiltration (Donnelly & Popovich 2008; Lee et al. 2009). Among these immune cells, some are neuroprotective, while others are destructive. The final outcomes of SCI depend on the dynamic balance of these cells (DiSabato et al. 2016; Wolf et al. 2002).

Previous studies found that local pro-inflammatory M1-type MG (MG) and/or infiltrated M1-type Mø are absolutely dominant following SCI (Fan et al. 2019; Sato et al. 2012). These suggest that M1 cells may be the key factor for the imbalance of local immune microenvironment of SCI. However, it remains controversial that these M1 cells are mainly from MG or the infiltrated Mø. Our recent research showed that the local M1 cells are mainly $CD45^{-/low}CD68^{+}CD11b^{+}$, rather than $CD45^{high}CD68^{+}CD11b^{+}$ cells in the subacute stage of SCI (Chen et al. 2021; Chen et al. 2020). In fact, CD45 is not only a common marker of peripheral leukocytes, it can also be expressed at a low level in MG (Sedgwick et al. 1998), CD11b is mainly expressed in MG and monocyte-derived Mø (Martin et al. 2017), and CD68 is the common marker of activated MG and Mø (Chen et al. 2015; Greaves & Gordon 2002). Therefore, $CD45^{high}CD68^{+}CD11b^{+}$ population was activated peripheral infiltrated Mø, $CD45^{-/low}CD68^{+}CD11b^{+}$ population was activated MG, and $CD45^{high}CD68^{-}CD11b^{-}$ population was peripheral infiltrated leukocytes excluding Mø. Thus, we speculated that the M1 cells in the injured spinal cords mainly derived from MG rather than infiltrating Mø. To test this hypothesis, in this study, the mouse SCI model was established, the activation and proportion of MG and infiltrated Mø at different time points following SCI were dynamically observed by a panel of specific cell markers using FCM and IHF.

Generally, in the rodent model, the pathological process of traumatic SCI is divided into the acute (< 48 h), subacute (2 to 14 dpi) and chronic (> 14 dpi) phases (Rodrigues et al. 2018; Shi et al. 2017). Therefore, in this study, we selected the sham-operated spinal cord as the normal control, 1 dpi as acute, 3, 7 and 14 dpi as subacute, 21 and 28 dpi as chronic phases, respectively. The results showed the proportions of total Mø/MG peaked at 7 dpi. Although, the proportions decreased at 14, 21 and 28 dpi, they were still maintained at high levels comparing with sham, 1 and 3 dpi. This change trend is consistent with the previous reports (Chen et al. 2015; Kigerl et al. 2009; Wang et al. 2015). We also found that the activated Mø increased significantly at 1 and 3 dpi following SCI. However, with the progression of pathological process, the activated MG dominated absolutely and increased nearly to 90% at 7, 14, 21 and 28 dpi. These demonstrate that in the early stage of SCI, the peripheral Mø infiltrate into the injured area rapidly, and the activated MG and Mø are in a roughly balanced state. This is consistent with previous report (Hellenbrand et al. 2021).

Here, we can find that the percentages of $CD68^{+}$ cells in 7, 14, 21 and 28 dpi groups were significant higher comparing with sham, 1 and 3 dpi groups, and there were no significant differences among 7, 14, 21 and 28 dpi groups. These may because in the later stage of subacute phase and chronic phase, most of the $CD68^{+}$ cells are activated MG and Mø, and their number

has reached the maximum. The possible reason is that lesion-associated factors (e.g., proinflammatory cytokines, oxygen tension, chemokines, etc.) persist indefinitely in the local microenvironment, and the recruitment of MG/Mø might promote new blood vessel growth and extracellular matrix deposition in these stages of SCI (Kigerl et al. 2009).

In this report, the activated MG are dominant at 7 dpi. Although, this is not consistent with previous report (Hellenbrand et al. 2021), it is consistent with the recent reports which using single-cell RNA sequencing to analyze the temporal changes at molecular and cellular leve ls in the injured mouse spinal cords (Li et al. 2022; Milich et al. 2021). The possible reason is that MG response following acute SCI limits infiltrated Mø dispersion (Plemel et al. 2020). Accordingly, we further found that both the proportions of M1 and M2 Mø were increased significantly at 1 and 3 dpi. However, they decreased to very low levels from 7 to 28 dpi. This phenomenon also shows that the activated MG might inhibit both infiltrated M1 and M2 Mø. Following SCI, the M1 MG increased and maintained at high levels from 7 to 28 dpi. On the contrary, the proportion of M2 MG decreased significantly after SCI and remained at a low level during the whole pathological process. Based on these results, we can infer that the activated MG are mainly M1 subtype following SCI. They inhibit not only the infiltration of peripheral monocytes, but also the polarization of these cells into M2 Mø. In the same way they can also inhibit the polarization of themselves into M2 MG. Therefore, M1 cells derived from MG are the key cells involved in proinflammatory response of SCI.

Following SCI, the main effector cells are the peripheral infiltrated Mø and resident MG (David & Kroner 2011). In fact, whether the immune response of these cells is good or bad depends on their subtypes and functional characteristics. Based on their functions, Mø/MG can be divided into M1 and M2 subtypes. M1 cells can damage nerve cells by secreting inflammatory cytokines, while M2 cells can regulate immune inflammatory response, remove necrotic tissue fragments, promote vascular regeneration, tissue reconstruction and repair (Kigerl et al. 2009; Kroner et al. 2014; Wang et al. 2015). In this study, we demonstrated that most Mø and MG in the injured spinal cords are M1 cells, only a small number showing M2 phenotype and they are transient. This shows that the predominance of M1 macroglia and lower number of M2 macroglia and/or Mø may contribute to the early inflammatory response and secondary damage following SCI. Therefore, for clinical transformation and application of Mø/MG, it is very necessary to determine the appropriate “time window” of these cells for immune intervention. Our temporal dynamic analysis suggests that the acute and early stage of subacute phase may be the "window period" for immune intervention targeting MG. During this “time window”, using effective intervention measures to timely inhibit the differentiation of MG into M1 subtype, rather than focusing on the infiltration and activation of peripheral monocytes, is of positive significance for increasing the proportion of M2 cells, improving the immune microenvironment and providing neuroprotection.

One limitation of this study is that the temporal dynamic analysis and the "window period" for immune intervention targeting MG only from mouse SCI model. Whether these laws are consistent with human related diseases still need to be further explored.

Conclusions

In summary, this study not only demonstrate that the pro-inflammatory M1 cells mainly come from MG rather than infiltrated Mø after SCI, but also determine their dynamic patterns. Therefore, these findings not only answer the academic debate about which of the infiltrating Mø

and MG plays a key role, but also determines the appropriate "time window" of immune intervention targeting M1-type MG for the treatment of SCI.

Data access

The study data are available in the supplementary files

References

Anjum A, Yazid MD, Fauzi Daud M, Idris J, Ng AMH, Selvi Naicker A, Ismail OHR, Athi Kumar RK, and Lokanathan Y. 2020. Spinal Cord Injury: Pathophysiology, Multimolecular Interactions, and Underlying Recovery Mechanisms. *Int J Mol Sci* 21. 10.3390/ijms21207533

Attal N. 2021. Spinal cord injury pain. *Rev Neurol (Paris)* 177:606-612. 10.1016/j.neurol.2020.07.003

Brockie S, Hong J, and Fehlings MG. 2021. The Role of Microglia in Modulating Neuroinflammation after Spinal Cord Injury. *Int J Mol Sci* 22. 10.3390/ijms22189706

Chay W, and Kirshblum S. 2020. Predicting Outcomes After Spinal Cord Injury. *Phys Med Rehabil Clin N Am* 31:331-343. 10.1016/j.pmr.2020.03.003

Chen J, Chen YQ, Shi YJ, Ding SQ, Shen L, Wang R, Wang QY, Zha C, Ding H, Hu JG, and Lu HZ. 2021. VX-765 reduces neuroinflammation after spinal cord injury in mice. *Neural Regen Res* 16:1836-1847. 10.4103/1673-5374.306096

Chen YJ, Zhu H, Zhang N, Shen L, Wang R, Zhou JS, Hu JG, and Lu HZ. 2015. Temporal kinetics of macrophage polarization in the injured rat spinal cord. *J Neurosci Res* 93:1526-1533. 10.1002/jnr.23612

Chen YQ, Wang SN, Shi YJ, Chen J, Ding SQ, Tang J, Shen L, Wang R, Ding H, Hu JG, and Lu HZ. 2020. CRID3, a blocker of apoptosis associated speck like protein containing a card, ameliorates murine spinal cord injury by improving local immune microenvironment. *J Neuroinflammation* 17:255. 10.1186/s12974-020-01937-8

David S, and Kroner A. 2011. Repertoire of microglial and macrophage responses after spinal cord injury. *Nat Rev Neurosci* 12:388-399. 10.1038/nrn3053

DiSabato DJ, Quan N, and Godbout JP. 2016. Neuroinflammation: the devil is in the details. *J Neurochem* 139 Suppl 2:136-153. 10.1111/jnc.13607

Donnelly DJ, and Popovich PG. 2008. Inflammation and its role in neuroprotection, axonal regeneration and functional recovery after spinal cord injury. *Exp Neurol* 209:378-388. 10.1016/j.expneurol.2007.06.009

Fan B, Wei Z, and Feng S. 2022. Progression in translational research on spinal cord injury based on microenvironment imbalance. *Bone Res* 10:35. 10.1038/s41413-022-00199-9

Fan B, Wei Z, Yao X, Shi G, Cheng X, Zhou X, Zhou H, Ning G, Kong X, and Feng S. 2018. Microenvironment Imbalance of Spinal Cord Injury. *Cell Transplant* 27:853-866. 10.1177/0963689718755778

Fan H, Tang HB, Chen Z, Wang HQ, Zhang L, Jiang Y, Li T, Yang CF, Wang XY, Li X, Wu SX, and Zhang GL. 2020. Inhibiting HMGB1-RAGE axis prevents pro-inflammatory macrophages/microglia polarization and affords neuroprotection after spinal cord injury. *J Neuroinflammation* 17:295. 10.1186/s12974-020-01973-4

Fan H, Tang HB, Shan LQ, Liu SC, Huang DG, Chen X, Chen Z, Yang M, Yin XH, Yang H, and Hao DJ. 2019. Quercetin prevents necroptosis of oligodendrocytes by inhibiting macrophages/microglia polarization to M1 phenotype after spinal cord injury in rats. *J Neuroinflammation* 16:206. 10.1186/s12974-019-1613-2

Gao ZS, Zhang CJ, Xia N, Tian H, Li DY, Lin JQ, Mei XF, and Wu C. 2021. Berberine-loaded M2 macrophage-derived exosomes for spinal cord injury therapy. *Acta Biomater* 126:211-223. 10.1016/j.actbio.2021.03.018

Greaves DR, and Gordon S. 2002. Macrophage-specific gene expression: current paradigms and future challenges. *Int J Hematol* 76:6-15. 10.1007/BF02982713

Hellenbrand DJ, Quinn CM, Piper ZJ, Morehouse CN, Fixel JA, and Hanna AS. 2021. Inflammation after spinal cord injury: a review of the critical timeline of signaling cues and cellular infiltration. *J Neuroinflammation* 18:284. 10.1186/s12974-021-02337-2

Hu JG, Shi LL, Chen YJ, Xie XM, Zhang N, Zhu AY, Jiang ZS, Feng YF, Zhang C, Xi J, and Lu HZ. 2016. Differential effects of myelin basic protein-activated Th1 and Th2 cells on the local immune microenvironment of injured spinal cord. *Exp Neurol* 277:190-201. 10.1016/j.expneurol.2016.01.002

Kigerl KA, Gensel JC, Ankeny DP, Alexander JK, Donnelly DJ, and Popovich PG. 2009. Identification of two distinct macrophage subsets with divergent effects causing either neurotoxicity or regeneration in the injured mouse spinal cord. *J Neurosci* 29:13435-13444. 10.1523/JNEUROSCI.3257-09.2009

Kilkenny C, Browne W, Cuthill IC, Emerson M, Altman DG, National Centre for the Replacement R, and Reduction of Amimals in R. 2011. Animal research: reporting in vivo experiments--the ARRIVE guidelines. *J Cereb Blood Flow Metab* 31:991-993. 10.1038/jcbfm.2010.220

Kroner A, Greenhalgh AD, Zarruk JG, Passos Dos Santos R, Gaestel M, and David S. 2014. TNF and increased intracellular iron alter macrophage polarization to a detrimental M1 phenotype in the injured spinal cord. *Neuron* 83:1098-1116. 10.1016/j.neuron.2014.07.027

Lee KD, Chow WN, Sato-Bigbee C, Graf MR, Graham RS, Colello RJ, Young HF, and Mathern BE. 2009. FTY720 reduces inflammation and promotes functional recovery after spinal cord injury. *J Neurotrauma* 26:2335-2344. 10.1089/neu.2008.0840

Li C, Wu Z, Zhou L, Shao J, Hu X, Xu W, Ren Y, Zhu X, Ge W, Zhang K, Liu J, Huang R, Yu J, Luo D, Yang X, Zhu W, Zhu R, Zheng C, Sun YE, and Cheng L. 2022. Temporal and spatial cellular and molecular pathological alterations with single-cell resolution in the adult spinal cord after injury. *Signal Transduct Target Ther* 7:65. 10.1038/s41392-022-00885-4

Ma SF, Chen YJ, Zhang JX, Shen L, Wang R, Zhou JS, Hu JG, and Lu HZ. 2015. Adoptive transfer of M2 macrophages promotes locomotor recovery in adult rats after spinal cord injury. *Brain Behav Immun* 45:157-170. 10.1016/j.bbi.2014.11.007

Mallon S, Kwiecien JM, and Karis JP. 2021. Imaging of Neurotrauma in Acute and Chronic Settings. *Curr Neuropharmacol* 19:1178-1190. 10.2174/1570159X19666210517114823

Martin E, El-Behi M, Fontaine B, and Delarasse C. 2017. Analysis of Microglia and Monocyte-derived Macrophages from the Central Nervous System by Flow Cytometry. *J Vis Exp*. 10.3791/55781

Milich LM, Choi JS, Ryan C, Cerqueira SR, Benavides S, Yahn SL, Tsoulfas P, and Lee JK. 2021. Single-cell analysis of the cellular heterogeneity and interactions in the injured mouse spinal cord. *J Exp Med* 218. 10.1084/jem.20210040

Mishra MK, Rawji KS, Keough MB, Kappen J, Dowlatabadi R, Vogel HJ, Chopra S, Distefano-Gagne F, Dufour A, Gosselin D, and Yong VW. 2021. Harnessing the Benefits of Neuroinflammation: Generation of Macrophages/Microglia with Prominent Remyelinating Properties. *J Neurosci* 41:3366-3385. 10.1523/JNEUROSCI.1948-20.2021

Perrouin-Verbe B, Lefevre C, Kieny P, Gross R, Reiss B, and Le Fort M. 2021. Spinal cord injury: A multisystem physiological impairment/dysfunction. *Rev Neurol (Paris)* 177:594-605. 10.1016/j.neurol.2021.02.385

Plemel JR, Stratton JA, Michaels NJ, Rawji KS, Zhang E, Sinha S, Baaklini CS, Dong Y, Ho M, Thorburn K, Friedman TN, Jawad S, Silva C, Caprariello AV, Hoghooghi V, Yue J, Jaffer A, Lee K, Kerr BJ, Midha R, Stys PK, Biernaskie J, and Yong VW. 2020. Microglia response following acute demyelination is heterogeneous and limits infiltrating macrophage dispersion. *Sci Adv* 6:eaay6324. 10.1126/sciadv.aay6324

Quadri SA, Farooqui M, Ikram A, Zafar A, Khan MA, Suriya SS, Claus CF, Fiani B, Rahman M, Ramachandran A, Armstrong IIT, Taqi MA, and Mortazavi MM. 2020. Recent update on basic mechanisms of spinal cord injury. *Neurosurg Rev* 43:425-441. 10.1007/s10143-018-1008-3

Rezvan M, Meknatkhah S, Hassannejad Z, Sharif-Alhoseini M, Zadegan SA, Shokraneh F, Vaccaro AR, Lu Y, and Rahimi-Movaghar V. 2020. Time-dependent microglia and macrophages response after traumatic spinal cord injury in rat: a systematic review. *Injury* 51:2390-2401. 10.1016/j.injury.2020.07.007

Rismanbaf A, Afshari K, Ghasemi M, Badripour A, Haj-Mirzaian A, Dehpour AR, and Shafaroodi H. 2021. Therapeutic Effects of Azithromycin on Spinal Cord Injury in Male Wistar Rats: A Role for Inflammatory Pathways. *J Neurol Surg A Cent Eur Neurosurg*. 10.1055/s-0041-1735854

Rodrigues LF, Moura-Neto V, and TCLS ES. 2018. Biomarkers in Spinal Cord Injury: from Prognosis to Treatment. *Mol Neurobiol* 55:6436-6448. 10.1007/s12035-017-0858-y

Sato A, Ohtaki H, Tsumuraya T, Song D, Ohara K, Asano M, Iwakura Y, Atsumi T, and Shioda S. 2012. Interleukin-1 participates in the classical and alternative activation of microglia/macrophages after spinal cord injury. *J Neuroinflammation* 9:65. 10.1186/1742-2094-9-65

Sedgwick JD, Ford AL, Foulcher E, and Airriess R. 1998. Central nervous system microglial cell activation and proliferation follows direct interaction with tissue-infiltrating T cell blasts. *J Immunol* 160:5320-5330.

Shi LL, Zhang N, Xie XM, Chen YJ, Wang R, Shen L, Zhou JS, Hu JG, and Lu HZ. 2017. Transcriptome profile of rat genes in injured spinal cord at different stages by RNA-sequencing. *BMC Genomics* 18:173. 10.1186/s12864-017-3532-x

Shields DC, Haque A, and Banik NL. 2020. Neuroinflammatory responses of microglia in central nervous system trauma. *J Cereb Blood Flow Metab* 40:S25-S33. 10.1177/0271678X20965786

Wang X, Cao K, Sun X, Chen Y, Duan Z, Sun L, Guo L, Bai P, Sun D, Fan J, He X, Young W, and Ren Y. 2015. Macrophages in spinal cord injury: phenotypic and functional change from exposure to myelin debris. *Glia* 63:635-651. 10.1002/glia.22774

Wolf SA, Fisher J, Bechmann I, Steiner B, Kwidzinski E, and Nitsch R. 2002. Neuroprotection by T-cells depends on their subtype and activation state. *J Neuroimmunol* 133:72-80. 10.1016/s0165-5728(02)00367-3

Zhang Y, Al Mamun A, Yuan Y, Lu Q, Xiong J, Yang S, Wu C, Wu Y, and Wang J. 2021. Acute spinal cord injury: Pathophysiology and pharmacological intervention (Review). *Mol Med Rep* 23. 10.3892/mmr.2021.12056

Zhao S, Kang R, Deng T, Luo L, Wang J, Li E, Luo J, Liu L, Wan S, and Zhao Z. 2018. Comparison of two cannulation methods for assessment of intracavernosal pressure in a rat model. *PLoS One* 13:e0193543. 10.1371/journal.pone.0193543

Figures

Figure 1 Flow chart of the pathway and whole idea of this research.

Figure 2 Temporal pattern of MG and infiltrated Mø following SCI detected by FCM.

A: The representative pictures of FCM in sham and injured spinal cords. B-L: The temporal pattern of the indicated cell populations after SCI. Data represent mean ± SD (n = 6). *$P < 0.05$,

593 $^{**}P < 0.01$ (Non-parametric Kruskal-Wallis ANOVA, following by the individual Mann-
594 Whitney U test).
595
596 **Figure 3 Temporal pattern of MG and infiltrated Mø following SCI detected by IHF.**
597
598 A-D: The representative pictures of TMEM119 (green) and CD11b (magenta) in the spinal
599 cords of sham and contusion epicentre at T9 segmental level (A: sham; B: 1 dpi; C: 7 dpi; D: 28
600 dpi). E and F: Quantitative analysis the cells of $CD11b^{+}TMEM119^{+}$(E) and $CD11b^{+}TMEM119^{-}$
601 (F). Data represent mean ± SD (n = 6). $^{*}P < 0.05$, $^{**}P < 0.01$. (Non-parametric Kruskal-Wallis
602 ANOVA, following by the individual Mann-Whitney U test).
603
604 **Figure 4 Temporal pattern of activated MG and infiltrated Mø following SCI detected by**
605 **IHF.**
606
607 A-D: The representative pictures of TMEM119 (green) and CD68 (magenta) in the spinal cords
608 of sham and contusion epicentre at T9 segmental level (A: sham; B: 1 dpi; C: 7 dpi; D: 28 dpi). E
609 and F: Cellular quantitation of $CD68^{+}TMEM119^{+}$(E) and $CD68^{+}TMEM119^{-}$ (F). Data represent
610 mean ± SD (n = 6). $^{*}P < 0.05$, $^{**}P < 0.01$. (Non-parametric Kruskal-Wallis ANOVA, following
611 by the individual Mann-Whitney U test).
612
613 **Figure 5 Temporal pattern of SCI-induced M1 and M2 differentiation of Mø and MG**
614 **detected by FCM.**
615 A, E and I: Representative images of total M1 and M2 cells (A), M1 and M2 MG (E), M1 and
616 M2 Mø (I) detected by FCM in sham and injured spinal cords. B-D, F-H and J-L: The temporal
617 pattern of the indicated cell populations after SCI. Data represent mean ± SD (n = 6). $^{*}P < 0.05$,
618 $^{**}P < 0.01$. (Non-parametric Kruskal-Wallis ANOVA, following by the individual Mann-
619 Whitney U test).
620
621 **Figure 6 Temporal pattern of SCI-induced differentiation of total M1 and M2 cells**
622 **following SCI detected by IHF.**
623
624 A-H: The representative pictures of CCR7 (green) and CD68 (magenta) (A-D), and Arg1 (green)
625 and CD68 (magenta) (E-H) in the spinal cords of sham and contusion epicentre at T9 segmental
626 level (A, E: sham; B, F: 1 dpi; C, G: 7 dpi; D, H: 28 dpi). I and J: Cellular quantitation of
627 $CD68^{+}CCR7^{+}$(I) and $CD68^{+}Arg1^{+}$(J). Data represent mean ± SD (n = 6). $^{*}P < 0.05$, $^{**}P < 0.01$.
628 (Non-parametric Kruskal-Wallis ANOVA, following by the individual Mann-Whitney U test).
629
630 **Figure 7 Temporal pattern of SCI-induced M1 and M2 differentiation of Mø and MG**
631 **following SCI detected by IHF.**
632
633 A-H: The representative pictures of CCR7 (green) and TMEM119 (magenta) (A-D), and Arg1
634 (green) and TMEM119 (magenta) (E-H) in the spinal cords of sham and contusion epicentre at
635 T9 segmental level (A, E: sham; B, F: 1 dpi; C, G: 7 dpi; D, H: 28 dpi). I-L: Cellular quantitation
636 of $TMEM119^{+}CCR7^{+}$ (I), $TMEM119^{+}Arg1^{+}$ (J) cells, infiltrated M1 Mø (K) and infiltrated M1
637 Mø (L). Data represent mean ± SD (n = 6). $^{*}P < 0.05$, $^{**}P < 0.01$. (Non-parametric Kruskal-
638 Wallis ANOVA, following by the individual Mann-Whitney U test).

Figure 8 Summary of dynamic changes of MG, infiltrated Mø and their subsets.

This is an integrated analysis of Figures 2-7. The first to seventh lines indicate sham, 1, 3, 7, 14, 21 and 28 dpi, respectively. The first row shows the proportions of total Mø/MG and the other cells. The second row shows the proportions of activated and resting cells in total Mø/MG. The third row shows the proportions of activated Mø and activated MG in the activated Mø/MG. The fourth row shows the proportion of M1 and M2 subsets in the activated MG and infiltrated Mø.

Tables

Table 1 Antibodies used in the study

Figure 1

Flow chart of the pathway and whole idea of this research

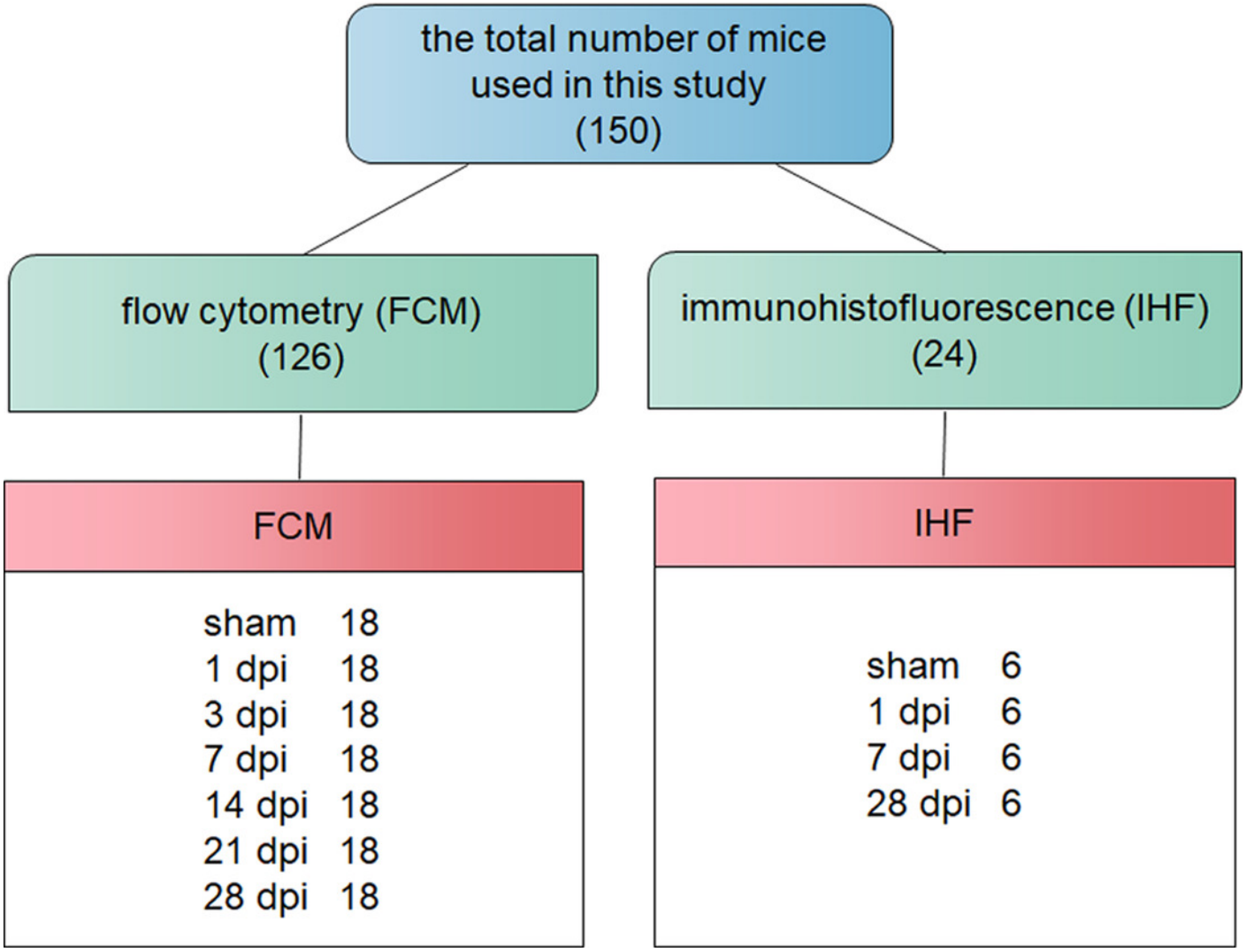

Figure 2

Temporal pattern of MG and infiltrated Mø following SCI detected by FCM

A: The representative pictures of FCM in sham and injured spinal cords. B-L: The temporal pattern of the indicated cell populations after SCI. Data represent mean ± SD (n = 6). *P < 0.05, **P < 0.01 (Non-parametric Kruskal-Wallis ANOVA, following by the individual Mann-Whitney U test).

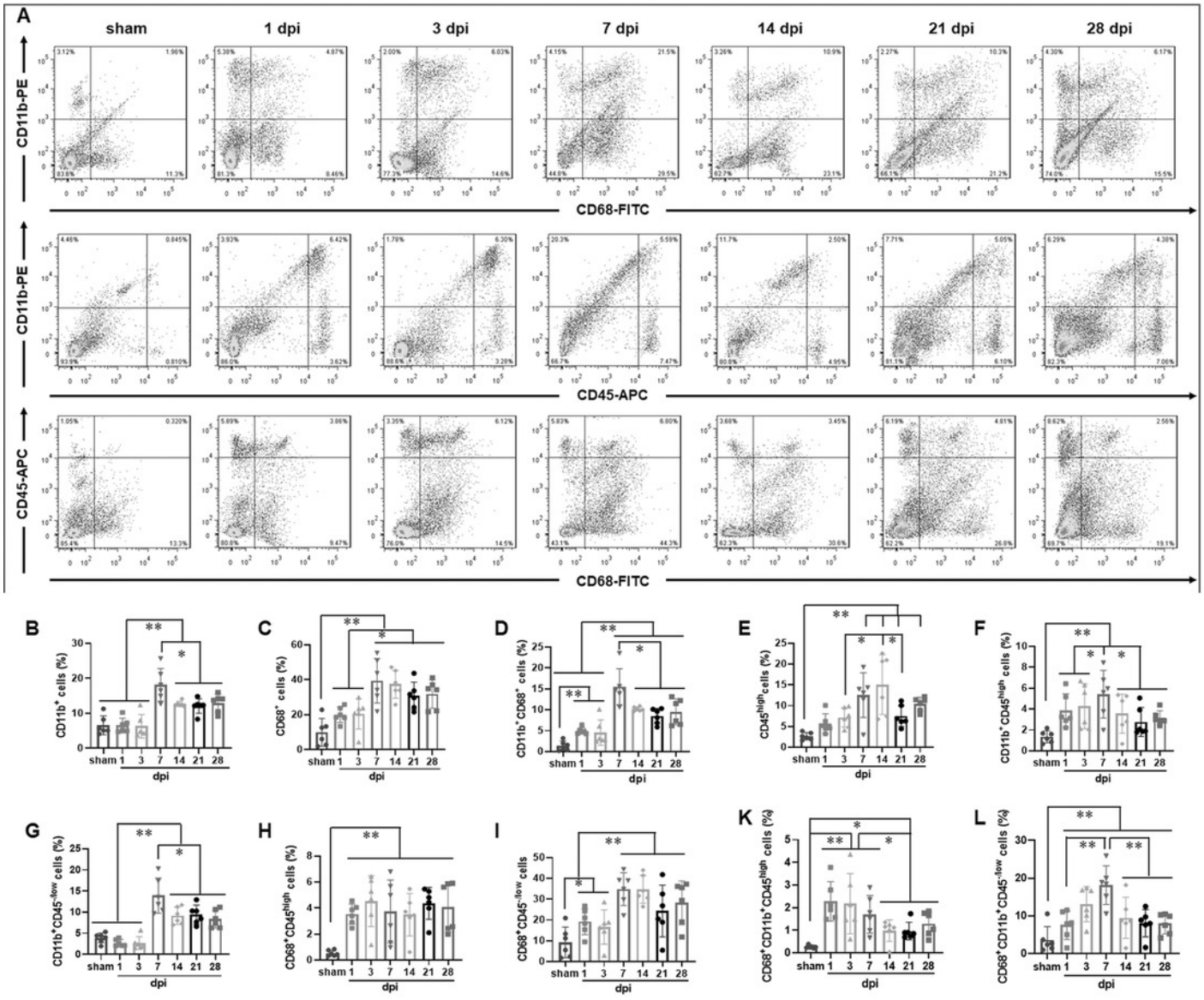

Figure 3

Temporal pattern of MG and infiltrated Mø following SCI detected by IHF

A-D: The representative pictures of TMEM119 (green) and CD11b (magenta) in the spinal cords of sham and contusion epicentre at T9 segmental level (A: sham; B: 1 dpi; C: 7 dpi; D: 28 dpi). E and F: Quantitative analysis the cells of $CD11b^{+}TMEM119^{+}$(E) and $CD11b^{+}TMEM119^{-}$(F). Data represent mean ± SD (n = 6). $*P < 0.05$, $**P < 0.01$. (Non-parametric Kruskal-Wallis ANOVA, following by the individual Mann-Whitney U test).

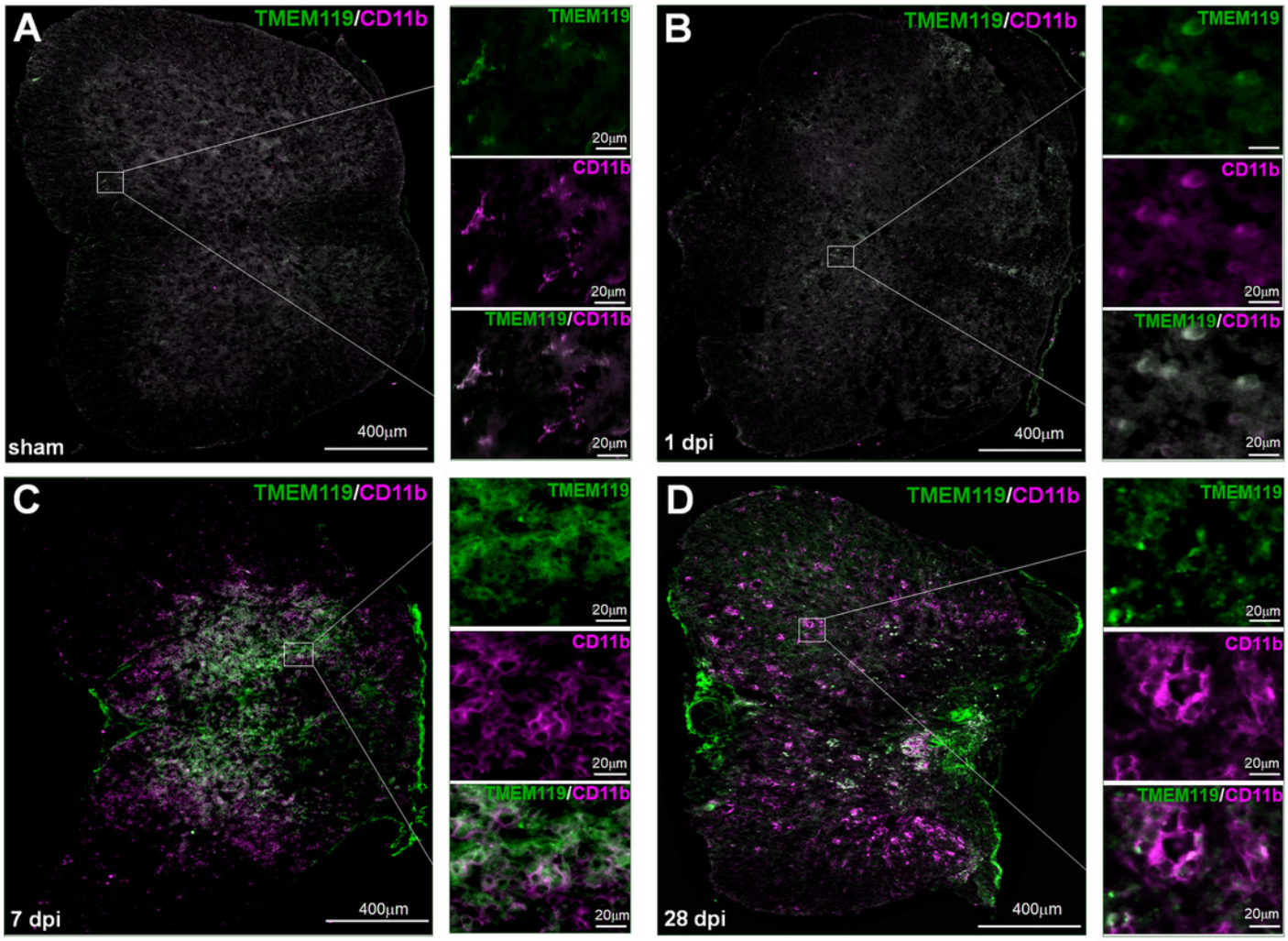
A
TMEM119/CD11b
TMEM119
20μm
CD11b
20μm
TMEM119/CD11b
20μm
sham
400μm
B
TMEM119/CD11b
TMEM119
CD11b
20μm
TMEM119/CD11b
20μm
1 dpi
400μm
C
TMEM119/CD11b
TMEM119
20μm
CD11b
20μm
TMEM119/CD11b
20μm
7 dpi
400μm
D
TMEM119/CD11b
TMEM119
20μm
CD11b
20μm
TMEM119/CD11b
20μm
28 dpi
400μm

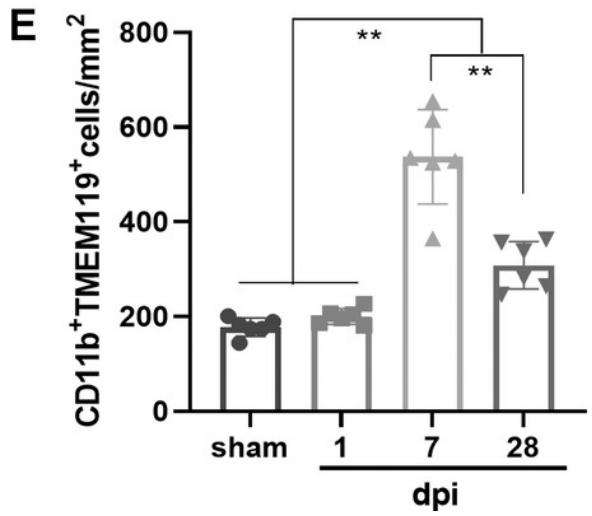
E
CD11b+TMEM119+cells/mm2
800
600
400
200
0
**
**
sham
1
7
28
dpi

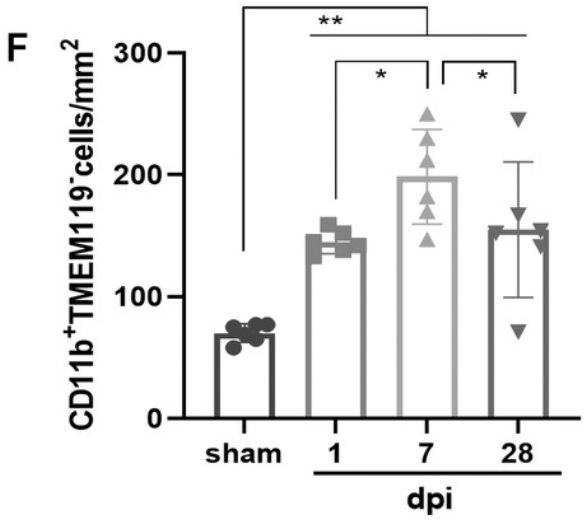
F
CD11b+TMEM119-cells/mm2
300
200
100
0
**
*
*
sham
1
7
28
dpi

Figure 4

Temporal pattern of activated MG and infiltrated Mø following SCI detected by IHF

A-D: The representative pictures of TMEM119 (green) and CD68 (magenta) in the spinal cords of sham and contusion epicentre at T9 segmental level (A: sham; B: 1 dpi; C: 7 dpi; D: 28 dpi). E and F: Cellular quantitation of $CD68^{+}TMEM119^{+}$(E) and $CD68^{+}TMEM119^{-}$ (F). Data represent mean ± SD (n = 6). *$P < 0.05$, **$P < 0.01$. (Non-parametric Kruskal-Wallis ANOVA, following by the individual Mann-Whitney U test).

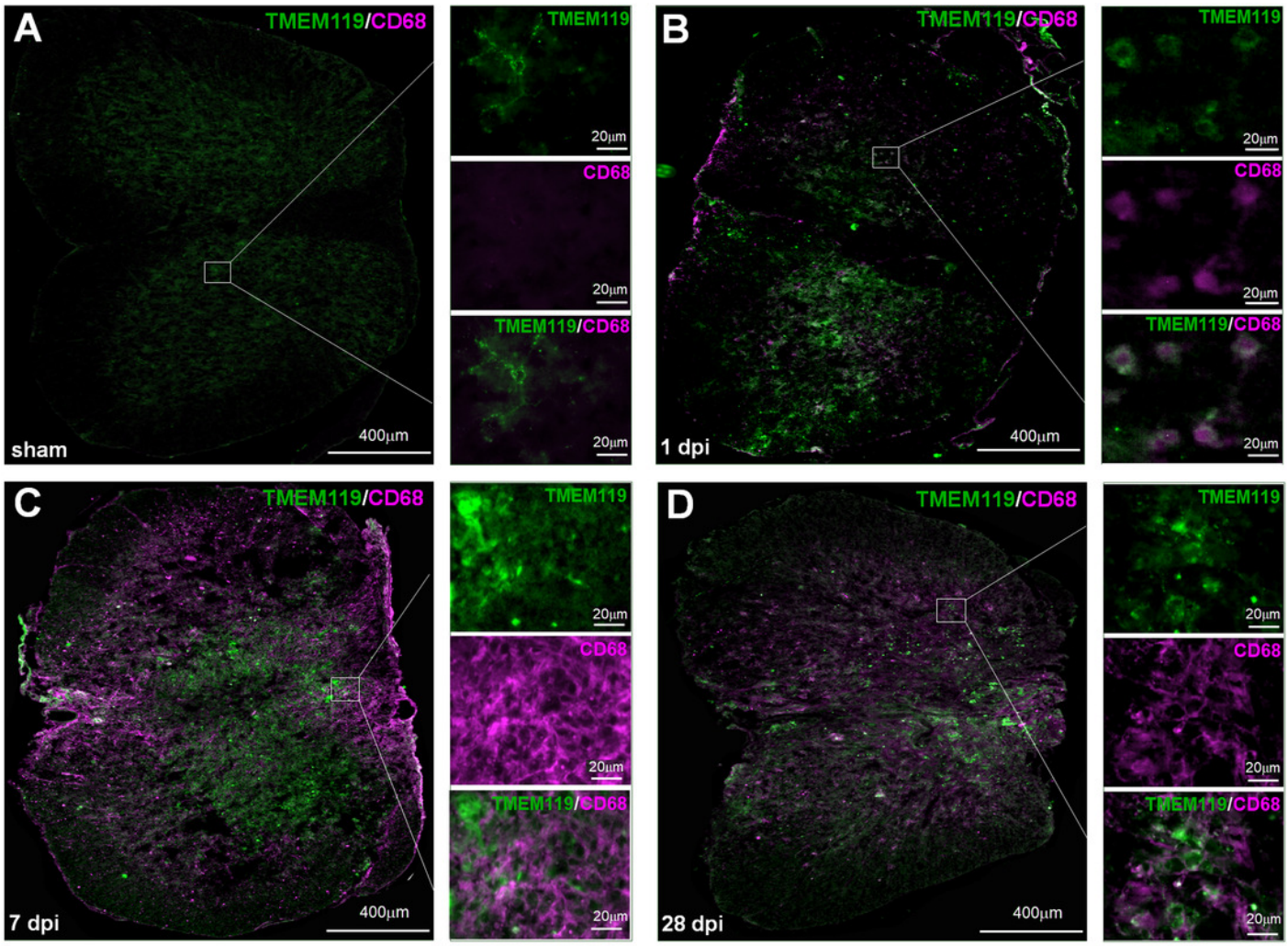
A
TMEM119/CD68
TMEM119
CD68
TMEM119/CD68
20μm
400μm
sham
B
1 dpi
C
7 dpi
D
28 dpi

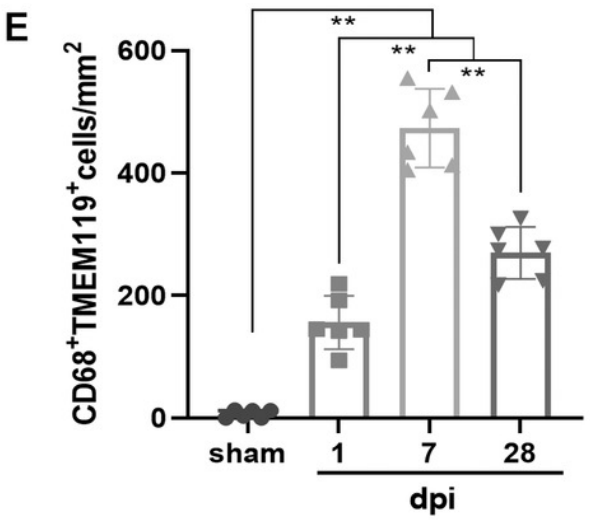
E
CD68+TMEM119+cells/mm2
600
400
200
0
**
sham
1
7
28
dpi

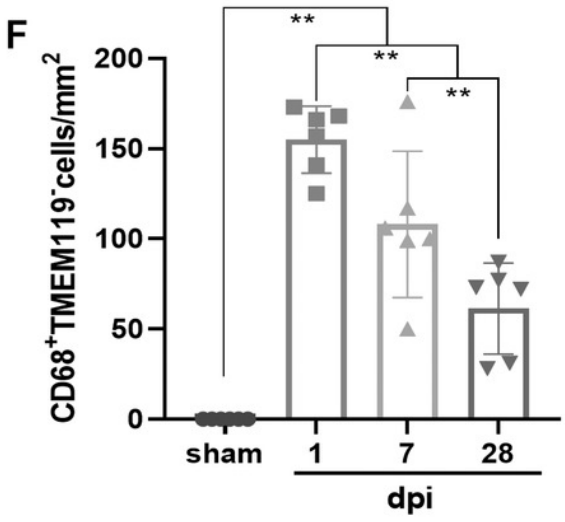
F
CD68+TMEM119-cells/mm2
200
150
100
50
0
**
sham
1
7
28
dpi

Figure 5

Temporal pattern of SCI-induced M1 and M2 differentiation of Mø and MG detected by FCM

A, E and I: Representative images of total M1 and M2 cells (A), M1 and M2 MG (E), M1 and M2 Mø (I) detected by FCM in sham and injured spinal cords. B-D, F-H and J-L: The temporal pattern of the indicated cell populations after SCI. Data represent mean ± SD (n = 6). *$P < 0.05$, **$P < 0.01$. (Non-parametric Kruskal-Wallis ANOVA, following by the individual Mann-Whitney U test).

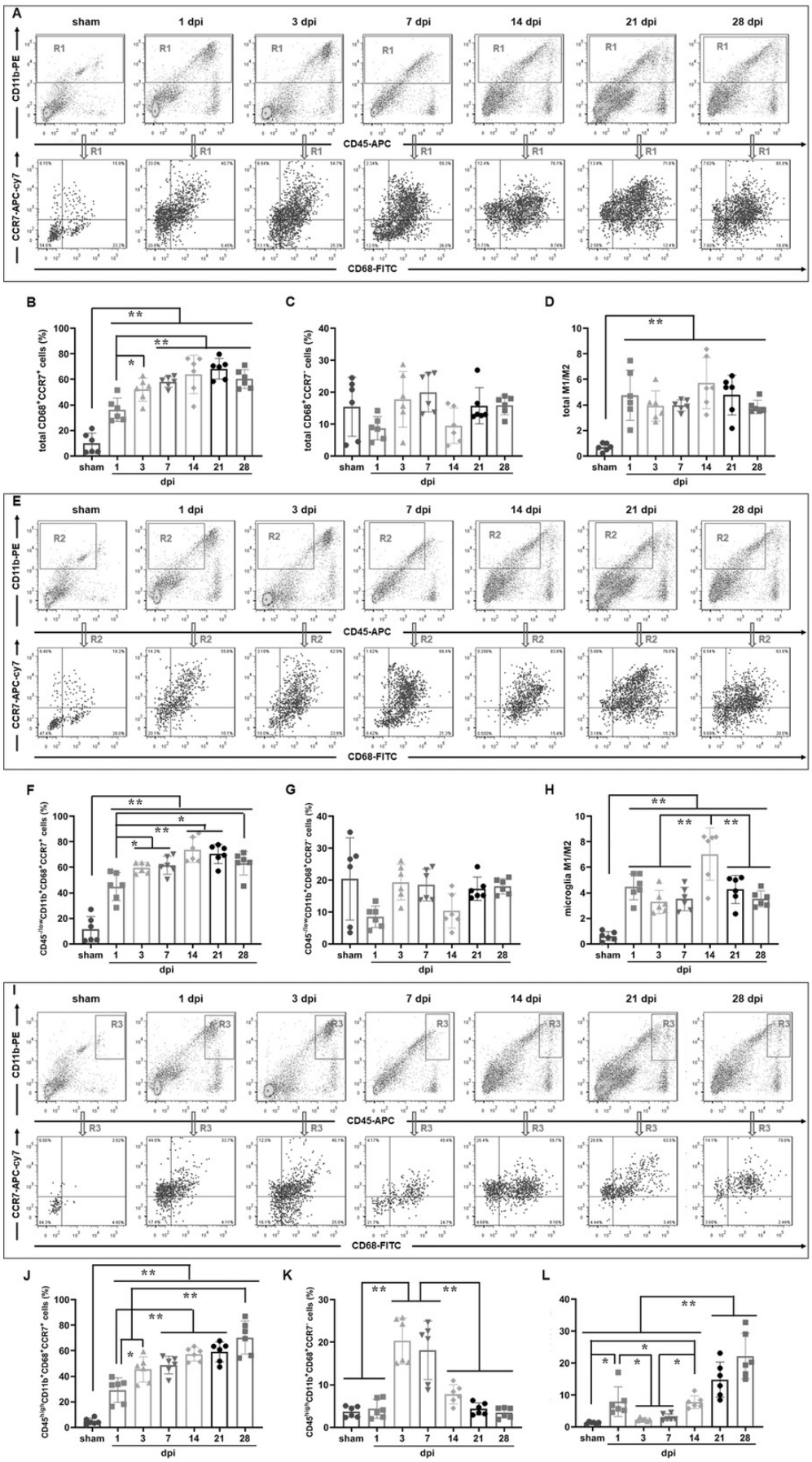
A
sham
1 dpi
3 dpi
7 dpi
14 dpi
21 dpi
28 dpi
CD11b-PE
CD45-APC
CCR7-APC-cy7
CD68-FITC
R1
B
total CD68+CCR7+ cells (%)
C
total CD68+CCR7- cells (%)
D
total M1/M2
dpi
E
R2
F
CD45high/lowCD11b+CD68+CCR7+ cells (%)
G
CD45high/lowCD11b+CD68+CCR7- cells (%)
H
microglia M1/M2
I
R3
J
CD45high/lowCD11b+CD68+CCR7+ cells (%)
K
CD45high/lowCD11b+CD68+CCR7- cells (%)
L

Figure 6

Temporal pattern of SCI-induced differentiation of total M1 and M2 cells following SCI detected by IHF

A-H: The representative pictures of CCR7 (green) and CD68 (magenta) (A-D), and Arg1 (green) and CD68 (magenta) (E-H) in the spinal cords of sham and contusion epicentre at T9 segmental level (A, E: sham; B, F: 1 dpi; C, G: 7 dpi; D, H: 28 dpi). I and J: Cellular quantitation of $CD68^{+}CCR7^{+}$(I) and $CD68^{+}Arg1^{+}$(J). Data represent mean ± SD (n = 6). $*P < 0.05$, $**P < 0.01$. (Non-parametric Kruskal-Wallis ANOVA, following by the individual Mann-Whitney U test).

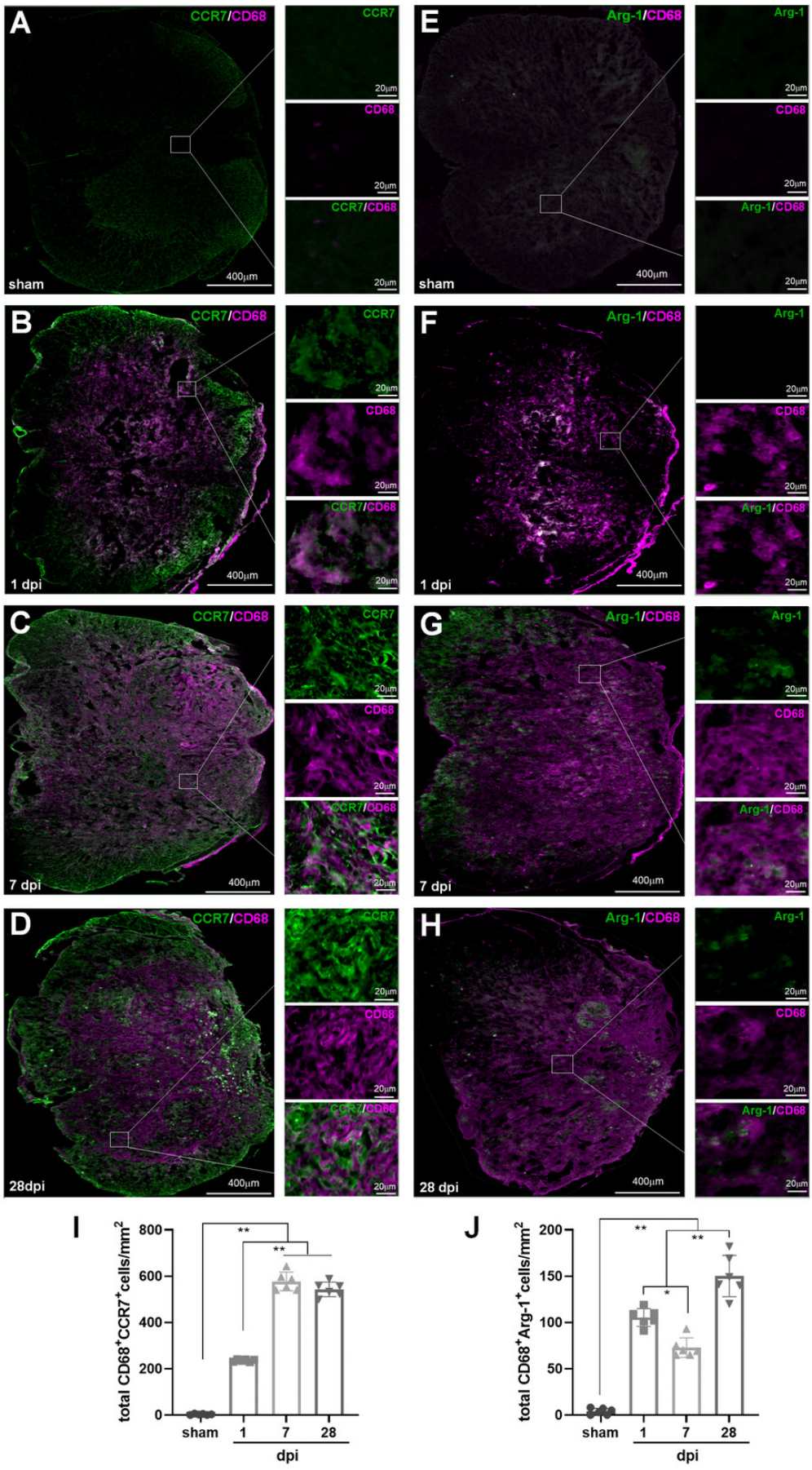
A
CCR7/CD68
CCR7
CD68
CCR7/CD68
sham
400μm
20μm
E
Arg-1/CD68
Arg-1
CD68
Arg-1/CD68
B
1 dpi
F
C
7 dpi
G
D
28dpi
H
28 dpi
I
total CD68+CCR7+cells/mm2
sham
1
7
28
dpi
J
total CD68+Arg-1+cells/mm2

Figure 7

Temporal pattern of SCI-induced M1 and M2 differentiation of Mø and MG following SCI detected by IHF

A-H: The representative pictures of CCR7 (green) and TMEM119 (magenta) (A-D) , and Arg1 (green) and TMEM119 (magenta) (E-H) in the spinal cords of sham and contusion epicentre at T9 segmental level (A, E: sham; B, F: 1 dpi; C, G: 7 dpi; D, H: 28 dpi). I-L: Cellular quantitation of $TMEM119^{+}CCR7^{+}$ (I), $TMEM119^{+}Arg1^{+}$ (J) cells, infiltrated M1 Mø (K) and infiltrated M1 Mø (L). Data represent mean ± SD (n = 6). *$P < 0.05$, **$P < 0.01$. (Non-parametric Kruskal-Wallis ANOVA, following by the individual Mann-Whitney U test).

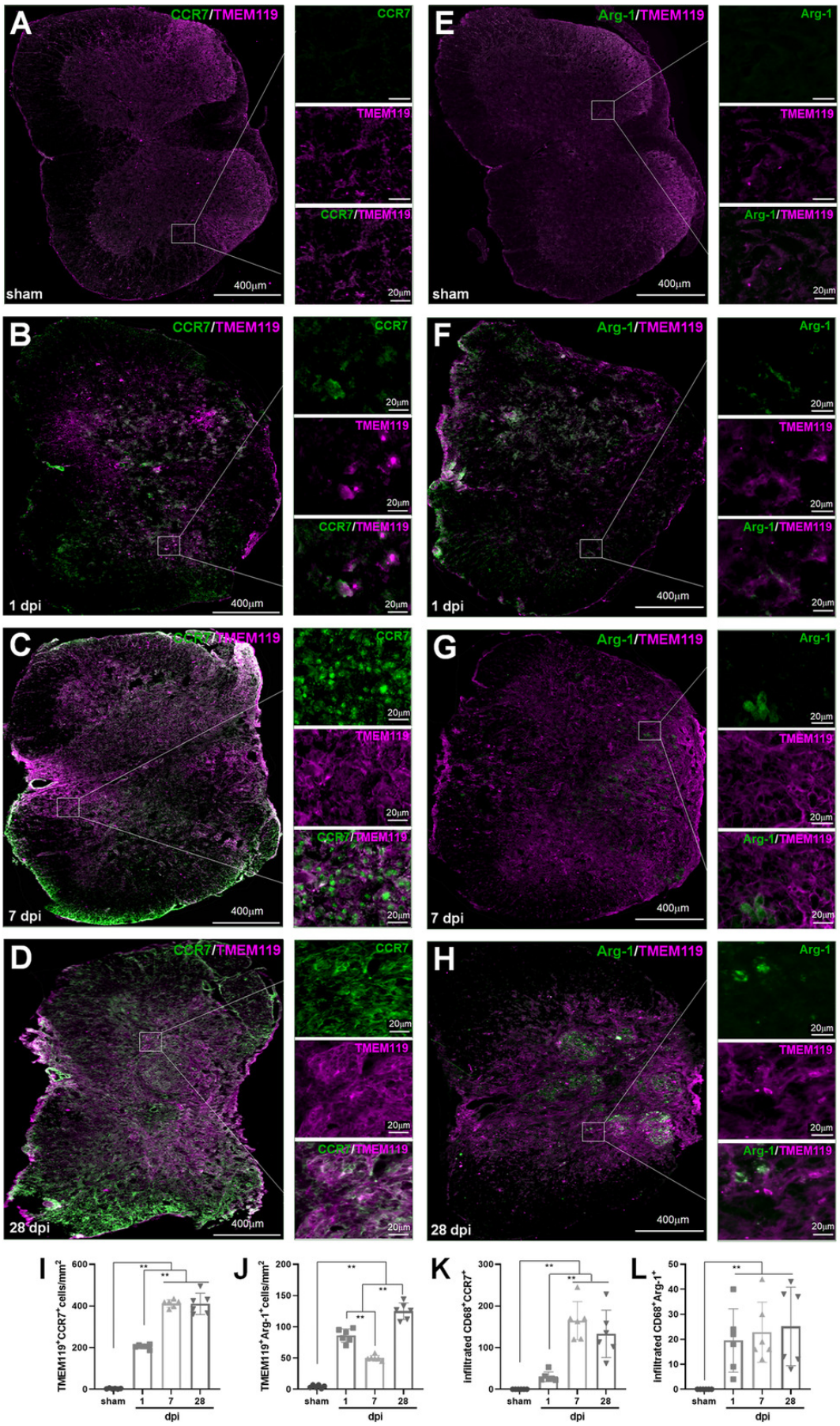
A
CCR7/TMEM119
CCR7
TMEM119
CCR7/TMEM119
sham
400μm
20μm
E
Arg-1/TMEM119
Arg-1
TMEM119
Arg-1/TMEM119
B
1 dpi
F
C
7 dpi
G
D
28 dpi
H
I
TMEM119+CCR7+ cells/mm2
J
TMEM119+Arg-1+ cells/mm2
K
Infiltrated CD68+CCR7+
L
Infiltrated CD68+Arg-1+
sham
1
7
28
dpi

Figure 8

Summary of dynamic changes of MG, infiltrated Mø and their subsets

This is an integrated analysis of Figures 2-7. The first to seventh lines indicate sham, 1, 3, 7, 14, 21 and 28 dpi, respectively. The first row shows the proportions of total Mø/MG and the other cells. The second row shows the proportions of activated and resting cells in total Mø/MG. The third row shows the proportions of activated Mø and activated MG in the activated Mø/MG. The fourth row shows the proportion of M1 and M2 subsets in the activated MG and infiltrated Mø.

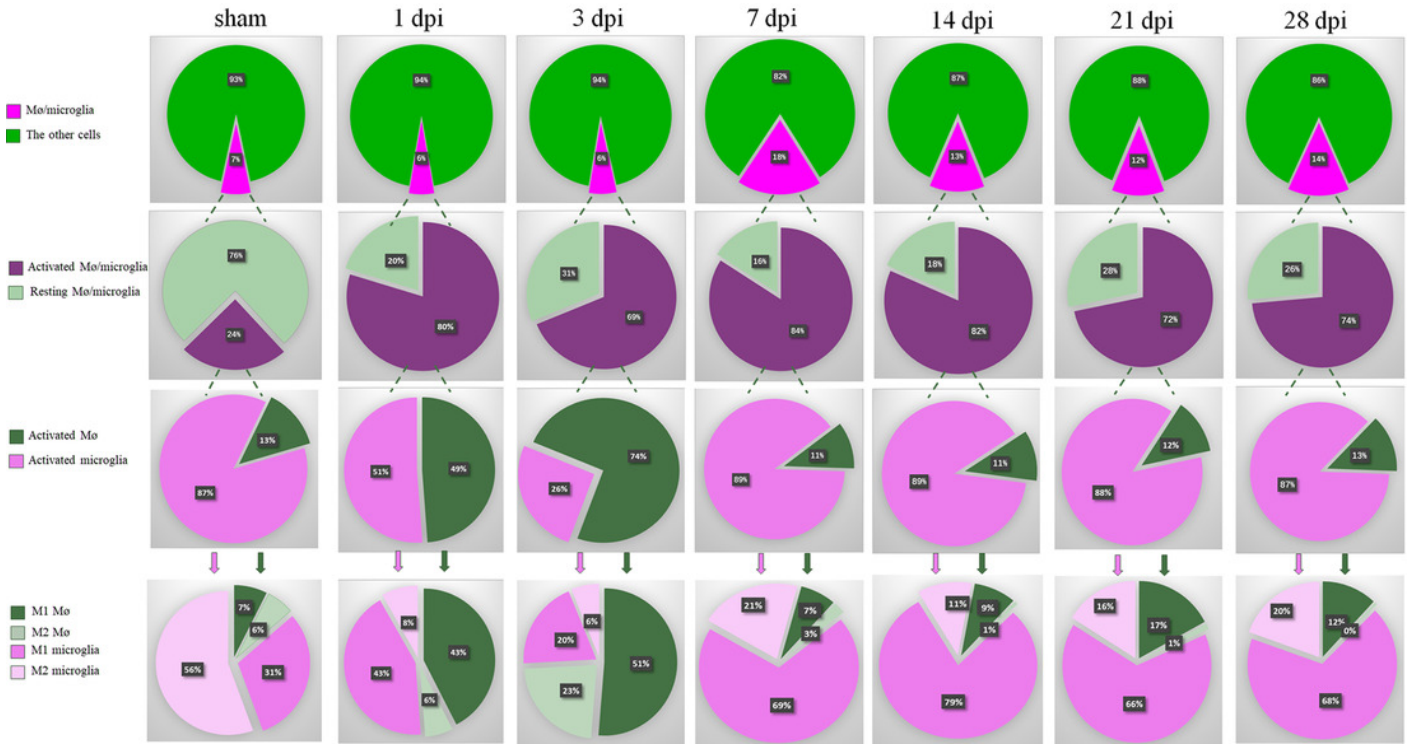

Table 1(on next page)

Antibodies used in the study

Antibodies used in the study

1 **Table 1 Antibodies used in the study**

2

Antigen	Host Species and Clone	Cat. # or Lot#	RRID	Conjugation	Source	Used concentration	Methods
CD11b	rat monoclonal	14-0112-82	AB_467108	NO	Invitrogen	1:200	IHF
CD45	rat monoclonal	14-0451-82	AB_467251				
CD68	rat monoclonal	MA5-16674	AB_2538168				
Arg1	rabbit polyclonal	PA5-29645	AB_2547120				
CCR7	rabbit polyclonal	ab191575			Abcam		
TMEM119	rat monoclonal	ab209064	AB_2800343				
Rat IgG (H+L)	goat polyclonal	112-095-143	AB_2338199	Fluorescein (FITC)	Jackson ImmunoResearch		
Rabbit IgG (H+L)	goat polyclonal	111-025-144	AB_2337932	Rhodamine (TRITC)			
CCR7	rat monoclonal	47-1971-82	AB_2573974	APC-eFluor 780 (AF780)	Invitrogen	0.25 μg/test	FCM
IgG2b kappa Isotype Control	rat	47-4321-82	AB_1271997				
CD11b	rat monoclonal	12-0112-81	AB_465546	PE		0.125 μg/test	
IgG2b kappa Isotype	rat	12-4031-82	AB_470042			0.25 μg/test	

Control							
CD68	rat monoclonal	MA5-16676	AB_2538170	FITC			
IgG2b kappa Isotype Control	rat	11-4031-82	AB_470004				
CD45	rat monoclonal	17-0451-82	AB_469392	APC		0.125 µg/test	
IgG2b kappa Isotype Control	rat	17-4031-82	AB_470176				

3